Chem. Senses 37: 553–566, 2012
doi:10.1093/chemse/bjs039
Advance Access publication April 2, 2012

A Computational Study of Odorant Transport and Deposition in the Canine Nasal Cavity: Implications for Olfaction

M. J. Lawson[1,2], B. A. Craven[1], E. G. Paterson[1] and G. S. Settles[2]

[1]Computational Mechanics Division, Applied Research Laboratory, The Pennsylvania State University, University Park, PA 16802 and [2]Gas Dynamics Laboratory, Mechanical and Nuclear Engineering Department, The Pennsylvania State University, University Park, PA 16802

Correspondence to be sent to: M.J. Lawson, National Renewable Energy Laboratory, National Wind Technology Center, 1617 Cole Boulevard, Mail Stop 3811, Golden, CO 80401, USA.

Accepted January 20, 2012

Abstract

Olfaction begins when an animal draws odorant-laden air into its nasal cavity by sniffing, thus transporting odorant molecules from the external environment to olfactory receptor neurons (ORNs) in the sensory region of the nose. In the dog and other macrosmatic mammals, ORNs are relegated to a recess in the rear of the nasal cavity that is comprised of a labyrinth of scroll-like airways. Evidence from recent studies suggests that nasal airflow patterns enhance olfactory sensitivity by efficiently delivering odorant molecules to the olfactory recess. Here, we simulate odorant transport and deposition during steady inspiration in an anatomically correct reconstructed model of the canine nasal cavity. Our simulations show that highly soluble odorants are deposited in the front of the olfactory recess along the dorsal meatus and nasal septum, whereas moderately soluble and insoluble odorants are more uniformly deposited throughout the entire olfactory recess. These results demonstrate that odorant deposition patterns correspond with the anatomical organization of ORNs in the olfactory recess. Specifically, ORNs that are sensitive to a particular class of odorants are located in regions where that class of odorants is deposited. The correlation of odorant deposition patterns with the anatomical organization of ORNs may partially explain macrosmia in the dog and other keen-scented species.

Key words: canine olfaction, computational fluid dynamics (CFD), nasal airflow, odorant deposition patterns, odorant transport

Introduction

Olfaction has traditionally been studied under the assumption that olfactory receptor neurons (ORNs) have free access to odorant molecules, thus ignoring the role that odorant transport from the external environment to ORNs in the nose may play in odor recognition. Nevertheless, there is a growing body of evidence that suggests that the pattern of odorant deposition in the nasal cavity (Mozell et al. 1991; Kent et al. 1996; Scott et al. 2006; Yang, Scherer, Zhao, et al. 2007) and the anatomical organization of ORNs (Vassar et al. 1993; Ressler et al. 1993; Strotmann et al. 1994; Mombaerts et al. 1996) play important roles in olfaction.

Mozell (1964, 1966, 1970) and Moulton (1976) were the first to describe "chromatographic" separation of odorants in the vertebrate nasal cavity, whereby odorant molecules are deposited nonuniformly along mucus-lined nasal airways. Recent experimental and computational studies have found that deposition patterns are odorant specific and depend on the nasal flow field as well as odorant solubility in the mucus layer (Kurtz et al. 2004; Zhao et al. 2006; Yang, Scherer, Zhao, et al. 2007). Furthermore, nonuniform odorant deposition influences the spatial response of the olfactory mucosa to an odorant stimulus (Mozell et al. 1987; Kent et al. 1996; Scott et al. 2006), suggesting that odorant deposition patterns play a role in odor recognition (Schoenfeld and Cleland 2005).

In macrosmatic mammals (e.g., carnivores, rodents, and marsupials), ORNs of the same type are expressed in rostral–caudal patterns that span out radially from the nasal septum to fill the nasal cavity (Ressler et al. 1993; Vassar et al. 1993; Strotmann et al. 1994; Mombaerts et al. 1996). Thus, the anatomical organization of ORNs in the olfactory epithelium also influences the response of the olfactory mucosa to an odorant stimulus (Mozell et al. 1987). Accordingly, the "composite" olfactory response is determined by both the

odorant deposition pattern "imposed" by the chromatographic effect and by the "inherent" ORN expression topography in the nasal cavity (Moulton 1976; Mozell et al. 1987).

Although ORN expression topography has not been mapped for the dog, expression topography has been extensively studied in the rat (Nef et al. 1992; Vassar et al. 1993; Miyamichi et al. 2005), which has a similar nasal anatomical structure (Negus 1958) and a comparable number of functional ORN types as the dog (Zhang and Firestein 2002; Quignon et al. 2005). Given the similarities in the nasal anatomy of canines and rats, the remainder of this paper will assume ORN organization is similar in both species unless otherwise noted. ORNs can generally be divided into 2 classes: class I and II. Class I ORNs are described as "fish-like" (Zhang and Firestein 2002) and are sensitive to highly soluble (hydrophilic) odorants that are rapidly absorbed in the mucus layer. Class II ORNs are more sensitive to insoluble (hydrophobic) odorants. In rats, class I ORNs cover approximately 25% of the nasal surface area and are expressed primarily in and around the dorsal meatus along the nasal septum, whereas class II ORNs are expressed across all olfactory surfaces (Mezler et al. 2001; Zhang et al. 2004; Schoenfeld and Knott 2004; Schoenfeld and Cleland 2005). Physiological measurements (electroolfactogram and voltage-sensitive dye visualization) corroborate this finding and show that odorant solubility and ORN expression patterns affect the response of the epithelium to an odorant stimulus (Kent et al. 1996, 2003; Kauer and White 2001). Additionally, recent electroolfactogram measurements show that highly soluble odorants evoke strong ORN activity along the nasal septum, whereas insoluble odorants produce a more uniform ORN response throughout the nasal cavity (Scott et al. 2006).

Craven et al. (2010) hypothesized that the nasal anatomical structure of macrosmatic animals, who rely on their sense of smell for survival, is optimized for efficient odorant delivery to ORNs in the sensory region of the nose (see also Schoenfeld and Cleland 2005). Craven et al. (2010) note that the sensory region in macrosmatic animals is relegated to an "olfactory recess" in the rear of the nasal cavity (see Negus 1958), which is bypassed by respiratory airflow. Moreover, the anatomical configuration of the olfactory recess in the dog was shown to force unidirectional laminar airflow during inspiration and a quiescent period during expiration (Craven et al. 2010). This unique airflow pattern combined with the large surface area for odorant absorption was proposed to enhance "chromatographic" separation patterns, which may aid in odor discrimination (Craven 2008; Craven et al. 2010). In contrast, microsmatic mammals (e.g., humans and primates) do not have such an olfactory recess and nasal airflow patterns in these species vary markedly from those in macrosmatic mammals. Thus, differences in nasal anatomy and resultant intranasal airflow patterns between microsmatic and macrosmatic species may lead to dramatically different odorant deposition patterns, which may partially explain differences in their olfactory abilities.

Objective

The dog possesses a highly developed nasal cavity (see Figure 1) and is widely considered to be one of nature's best chemical trace detectors (Settles 2005). Although several studies have investigated odorant transport in the nasal airways of rodents (Kimbell et al. 1993, 1997; Zhao et al. 2006; Yang, Scherer, Zhao, et al. 2007) and humans (Hahn et al. 1994; Keyhani et al. 1997; Kimbell et al. 2001; Zhao et al. 2004, 2006), odorant transport in the canine nose has not been studied to date.

Here, we use a high-fidelity computational fluid dynamics (CFD) model of the canine nasal cavity to simulate odorant transport from the external environment to ORNs at the epithelial surface. The objective of this study is to understand how nasal airflow influences odorant deposition patterns and to determine if deposition patterns correspond with ORN expression topography in a way that may enhance the dog's olfactory abilities.

Materials and methods

The canine specimen and nasal histology

This study was performed using an anatomically correct computer model of the left nasal cavity of a 29.5 kg mixed-breed female Labrador retriever cadaver. The computer model, presented in Figure 1, was reconstructed from high resolution ($180 \times 180 \times 200$ μm) magnetic resonance imaging (MRI) scans. Figure 2 illustrates the anatomy of the nasal cavity and shows the approximate locations of respiratory and olfactory epithelium. Herein, the respiratory and olfactory regions are defined as regions in the nasal cavity where respiratory and olfactory epithelium is found, respectively. The olfactory epithelium, which exclusively contains ORNs (Buck and Axel 1991), is confined to the ethmoidal region (olfactory region) of the nasal cavity, where it lines the bony scrolls known as ethmoturbinates (Evans and Miller 1993). Other nasal surfaces are covered with nonsensory respiratory epithelium

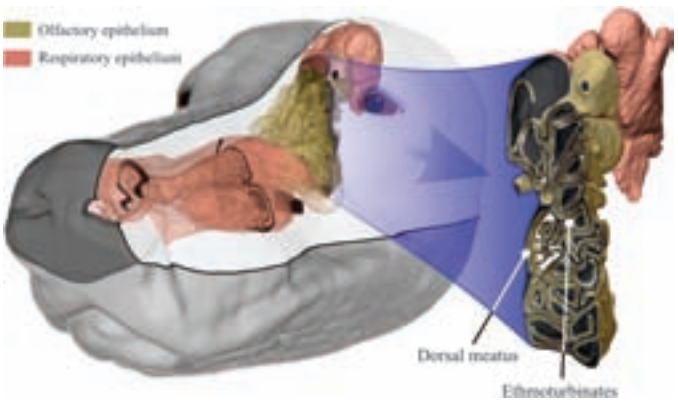

Figure 1 The computer model of the canine nasal airway.

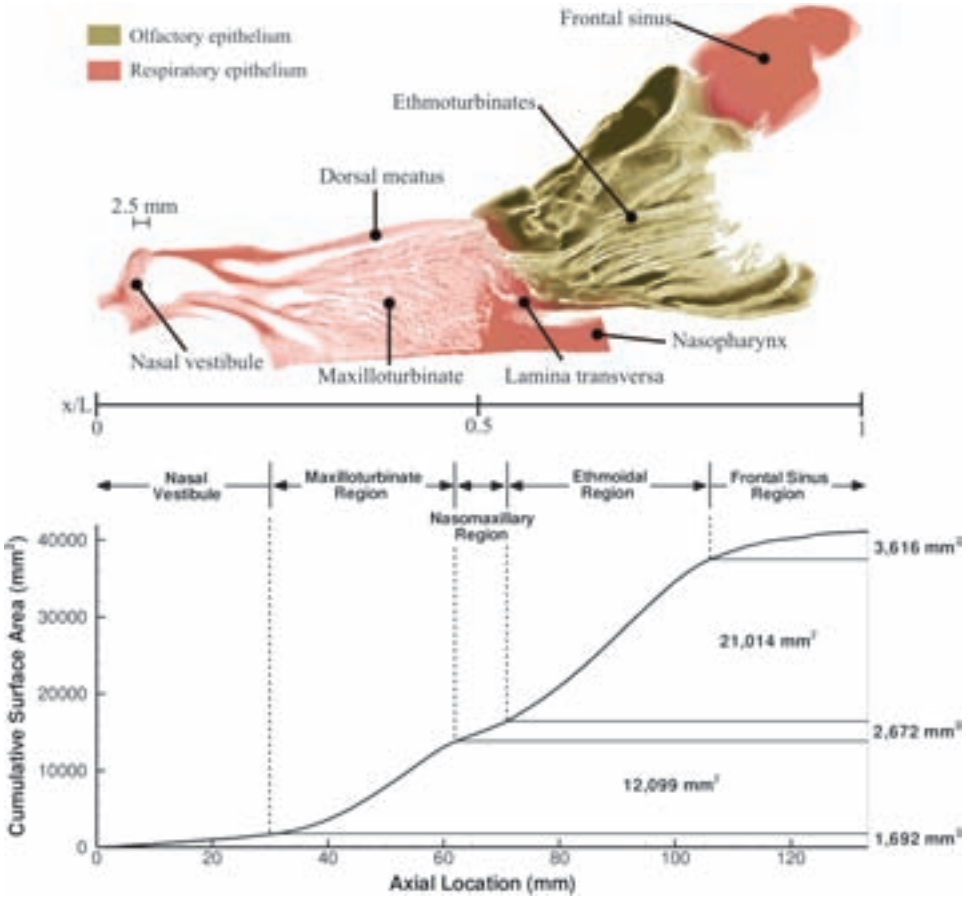

Figure 2 The canine nasal anatomy. (Top) A sagittal cross section of the nasal cavity illustrating the anatomical features of the nose. (Bottom) Distribution of cumulative surface area along the longitudinal axis of canine nasal airway. For reference, the volume of the nasal cavity is 0.24 L.

(Negus 1958; Evans and Miller 1993). The respiratory and olfactory regions are separated by the lamina transversa, and the dorsal meatus is the only direct pathway from the nasal vestibule to the olfactory recess. For more detail on the canine nasal anatomy and the methodology used to create the reconstructed model the reader is referred to Craven et al. (2007).

Generation of an anatomically correct computational mesh

The complexity of the canine nasal airway precluded the use of structured computational meshing techniques. Instead, a semiautomated octree-based method (*Harpoon*, Sharc Ltd.) was used to generate a 104-million-element hexahedral-dominant mesh that also contained wedge, pyramid, and tetrahedral elements (Craven et al. 2009). Figure 3 shows the computational domain, including illustrations of the mesh resolution achieved in the respiratory and olfactory airways.

Airflow solution

Craven et al. (2009) performed high-fidelity steady state CFD simulations of canine nasal airflow using the computer model of the canine nasal anatomy presented in Figure 1. Craven et al. (2009) provide a thorough discussion of the numerical methods and boundary conditions that were used, thus, only a brief overview is given here.

The majority of the canine nasal airflow has a Reynolds number on the order of 100 (Craven et al. 2007, 2009). Thus, turbulence was not considered in the airflow simulations. Additionally, buoyancy effects caused by the heating and humidification of inspired air are negligible compared with inertial and viscous effects and were not considered. Under this set of assumptions, the steady incompressible Navier–Stokes equations govern airflow through the nose and were solved over the computational mesh using the commercial CFD code *Acusolve* (ACUSIM Software Inc.).

Physiologically realistic nasal airflow rates during olfactory sniffing (i.e., airflow rates when the dog is sniffing to detect an odor as opposed to the flow rate during normal breathing), determined through a set of live-animal experiments (Craven et al. 2010), were used as boundary conditions for the airflow simulations. Airflow rates of 11% (50 mL/s), 48% (220 mL/s), and 100% (460 mL/s) of the maximum inspiratory value during olfactory sniffing were simulated. The

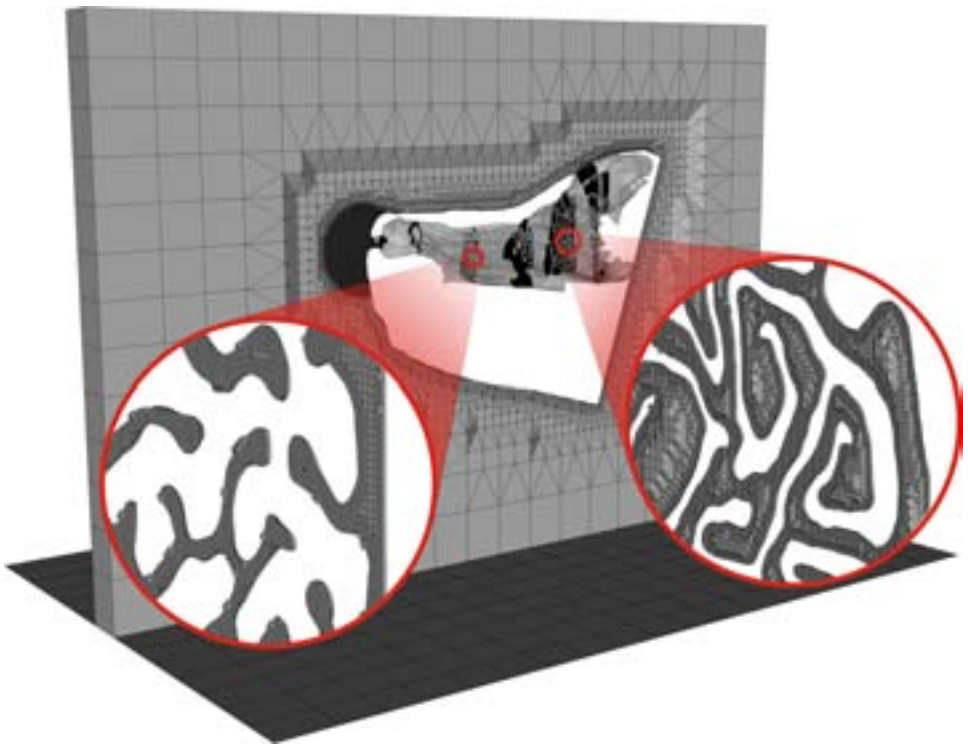

Figure 3 The computational domain. The mesh resolution in the respiratory (left) and olfactory (right) regions of the nasal cavity are shown.

nasal airways were given a no-slip boundary condition and a zero-gradient velocity condition was prescribed on the edges of the computational domain shown in Figure 3. A pressure differential was specified across the nose to drive the airflow.

Mathematical model of odorant transport in the nasal cavity

To solve the odorant transport problem, we implemented a modified form of a mathematical model first described by Hahn et al. (1994) and later modified by Craven (2008). The computational model accounts for the following phenomena: 1) advective–diffusive transport of odorant-laden air from the external environment through the nasal airways, 2) sorption of odorant into the mucus layer, 3) diffusion of odorant through the mucus layer toward the epithelial surface, and 4) consumption of odorant at the epithelial surface. The numerical solution of this mathematical model yields the odorant surface flux to ORNs and the odorant concentration profile in the olfactory recess.

Odorant transport in the nasal airways

Nasal airflow is responsible for transporting odorant molecules from the external environment to the olfactory recess. In the vapor phase, odorants are transported as passive scalars in the nasal airstream as governed by the advection–diffusion equation:

$$u_i \frac{\partial C_a}{\partial x_i} = D_{oa} \frac{\partial C_a}{\partial x_i \partial x_i}. \quad (1)$$

Here, u_i is the airstream velocity, D_{oa} is the binary diffusion coefficient of odorant in air, and C_a is the nondimensional air-phase odorant concentration.

The Péclet number, $Pe_a = \frac{U_a L}{D_{oa}}$, is a nondimensional parameter that characterizes the competing effects of advective and diffusive transport phenomena. In the canine nose, $U_a \sim 1$–10 m/s is a characteristic velocity, $L \sim 0.001$ m is the characteristic airway diameter, and $D_{oa} \sim 1 \times 10^{-5}$ m^2/s, resulting in $Pe_a \gg 1$. This indicates that advection is the dominant mechanism by which odor molecules are transported into the olfactory recess.

Odorant sorption at the air–mucus interface

As odorant-laden air flows through the olfactory recess, odorant sorption occurs at the air–mucus interface, whereby odorant molecules enter the mucus layer. Figure 4 presents a schematic illustration of the transport phenomena that occur during this process. Henry's Law (eq. 2) and conservation of mass (eq. 3) govern odorant transport across the air–mucus interface:

$$C_a\big|_{x_n=0} = K_p C_m\big|_{x_n=0,} \tag{2}$$

$$D_{oa}\frac{\partial C_a}{\partial x_n}\Big|_{x_n=0} = D_{om}\frac{\partial C_m}{\partial x_n}\Big|_{x_n=0.} \tag{3}$$

Here, C_m is the odorant concentration in the mucus layer, D_{om} is the binary diffusion coefficient of odorant in the mucus layer, and K_p is the equilibrium partition coefficient, a measure of odorant solubility. x_n is the direction normal to the air–mucus interface.

Henry's Law permits a discontinuous jump in odorant concentration across the air–mucus interface. Most odorants have an air–mucus partition coefficient smaller than 1, which amplifies the mucus-phase odorant concentration across the air–mucus interface. Table 1 contains the properties of the odorants considered in this study. The partition coefficients of the odorants considered here span 6 orders of magnitude, ranging from insoluble limonene to highly soluble dinitrotoluene (DNT). During steady inspiration, odorant transport through the nasal airways is a function of the air flow field alone, thus the relative difference in partition coefficients between odorants causes the odorant-specific deposition patterns that have been observed in the nasal cavity (see Mozell et al. 1987; Kent and Mozell 1992; Zhao et al. 2006; Yang, Scherer, Zhao, et al. 2007).

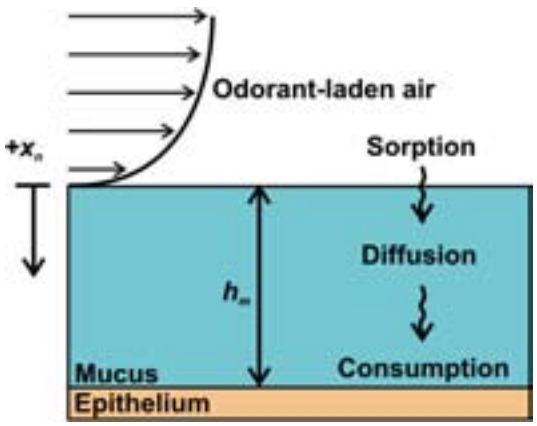

Figure 4 Schematic illustration of the transport phenomena occurring at the air–mucus interface and within the mucus layer. h_m is the mucus layer thickness in the olfactory recess. Note that ORNs that bind odorant molecules are located at the epithelial surface.

Odorant transport across the mucus layer

In the mucus layer, odorant molecules diffuse through the approximately stagnant mucus to ORN binding sites embedded within the plasma membrane of the sensory cilia that cover the olfactory epithelial surface. Diffusion parallel to the air–mucus interface is neglected because of the thinness of the mucus layer ($h_m \sim 10$ μm; Menco 1980) relative to the length of the nasal cavity ($L = 0.13$ m). Odorant transport in the mucus layer is therefore assumed to be 1D and normal to the air–mucus interface as described by the 1D diffusion equation.

Odorant binding at the epithelial surface

Once odorant molecules reach the epithelial surface, they are bound by G protein–coupled olfactory receptors embedded in the cilia membranes. The dwell time of odorant molecules at the receptor site is on the order of 1 ms (Bhandawat et al. 2005). After being bound, odorant molecules are quickly consumed, presumably by odorant-degrading enzymes (Pelosi 1996), odorant-binding proteins (Steinbrecht 1998; Briand et al. 2002), or vascular clearance (Hahn et al. 1994).

The time required for odorant molecules to diffuse through the mucus layer is on the order of 0.1 s (Craven 2008), much longer than the dwell time at the olfactory receptor sites. Consequently, from the perspective of a diffusing molecule, odorants are instantaneously bound and consumed by olfactory receptors as they reach the epithelial surface. Thus, if the olfactory receptors do not become saturated with odorant molecules, the effective odorant concentration at the epithelial surface is zero (Truskey et al. 2008). This scenario, known as diffusion-limited binding, is physiologically realistic in the case of weak odor signals, where the rate of odorant binding and clearance is much faster than the rate of odorant diffusion through the mucus layer toward the epithelial surface. Here, we consider the case of diffusion-limited binding.

Table 1 Chemical proprieties of the odorants considered

Odorant	Molecular formula	K_p	D_{oa} (m^2/s)	D_{om} (m^2/s)	θ	Solubility
Limonene	$C_{10}H_{16}$	1.05	6.30×10^{-6}	7.00×10^{-10}	$1.06 \times 10^{+1}$	Low
n-Amyl acetate	$C_7H_{14}O_2$	1.59×10^{-2}	6.70×10^{-6}	7.80×10^{-10}	$7.32 \times 10^{+2}$	Moderate
2,4-Dinitrotoluene (DNT)	$C_7H_6N_2O_4$	2.21×10^{-6}	6.50×10^{-6}	7.30×10^{-10}	$5.08 \times 10^{+6}$	High

Air–mucus partition coefficients (K_p) were estimated using air–water Henry's Law constants determined using HENRYWIN version 3.20 (US Environmental Protection Agency, Estimation Program Interface Suite, http://www.epa.gov/oppt/exposure/pubs/episuite.htm). Odorant diffusion coefficients in air and mucus, D_{oa} and D_{om}, respectively, were determined using the Environmental Protection Agency's On-line Tools for Site Assessment Calculation (http://www.epa.gov/athens/learn2model/part-two/onsite/estdiffusion-ext.html). θ is a nondimensional parameter that describes how readily odorant molecules are transported from the airstream to the epithelial surface (see section *Odorant transport boundary conditions on nasal surfaces*). Note that θ values were calculated using a mucus layer thickness of $h_m = 10$ μm (Menco 1980).

Numerical solution of the mathematical model

Given the previously verified airflow solutions (Craven et al. 2009), the commercial CFD software package *Acusolve* (ACUSIM Software Inc., see Hughes et al. 1986; Shakib 1989) was used to solve equation (1) for odorant transport over the computational mesh of the canine nasal cavity. Simulations were performed with each odorant listed in Table 1 for nasal airflow rates given in the *Airflow solution* section. The nondimensional odorant concentration entering the nose was set to $C_a = 1$ for all simulations. Since expiratory airflow completely bypasses the olfactory recess during sniffing (see Craven et al. 2010, Figure 5c), this phase of a sniff has no effect on odorant deposition patterns in the olfactory recess and was therefore not considered in the present study. The odorant transport phenomena in the mucus layer covering the nasal cavity were simulated using the air-phase boundary conditions described in the following section.

Odorant transport boundary conditions on nasal surfaces

Previous CFD simulations (see the Results section and Craven et al. 2009) have shown that only the mucus-coated dorsal meatus delivers airflow to the olfactory region of the dog's nose. Airflow through all other respiratory airways completely bypasses the olfactory region (Craven et al. 2009), thus odorant deposition in these airways is irrelevant to olfaction (although certainly still relevant in toxicology and other concerns beyond the present scope). Therefore, in order to simplify the present CFD simulations, we only simulated odorant transport along the dorsal meatus and in the olfactory recess. All other airways were given a zero-odorant-flux boundary condition,

$$\frac{\partial C_a}{\partial x_n}\Big|_{x_n=0} = 0. \quad (4)$$

Preliminary simulations were performed to verify that this simplification did not affect the results. These preliminary simulations are discussed later in this section.

It is important to note that although the nasal vestibule leads to the dorsal meatus on inspiration, it is covered with skin-like squamous epithelium, which has a very low permeability in comparison to the mucus-lined respiratory and olfactory epithelium (Kimbell et al. 2001). As such, using equation (4) as the boundary condition for the nasal vestibule is assumed to introduce negligible uncertainty in the solution.

In general, to simulate odorant transport along the dorsal meatus and in the olfactory recess, transport in the air and mucus phases must be simulated simultaneously using equations (2) and (3) to couple the solutions across the air–mucus interface. To simplify the solution procedure for steady state simulations, mucus layer transport was reduced to an air-phase boundary condition using a method first demonstrated by Keyhani et al. (1995). At steady state, according to the present assumptions, the odorant concentration profile is linear across the mucus layer with a concentration of zero at the epithelial surface. Combining this linear profile with equations (2) and (3) results in equation (5), an air-phase boundary condition that accounts for odorant sorption, diffusion, and consumption in the mucus layer. Equation (5) was applied as a boundary condition on all olfactory surfaces in the

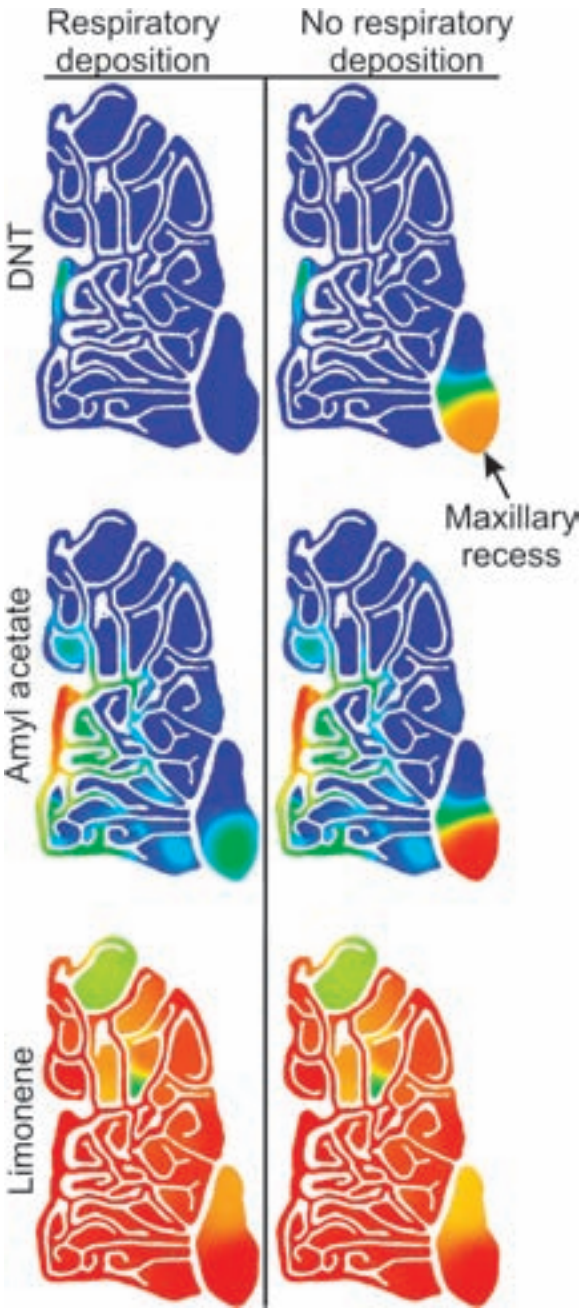

Figure 5 Odorant transport patterns in a transverse section through the olfactory region of the dog's nose for (left) simulations where odorant deposition in the respiratory airways was modeled and (right) simulations in which the respiratory airways were given a zero-odorant-flux boundary condition. The airflow rate is 220 mL/s.

nose (see Figures 1 and 2). We also assume that odorant uptake along the mucus-lined dorsal meatus can be simulated using this boundary condition:

$$\left.\frac{\partial C_a}{\partial x_n}\right|_{x_n=0} + \theta C_a\big|_{x_n=0} = 0, \tag{5}$$

$$\theta = \frac{D_{om}}{D_{oa} h_m K_p}. \tag{6}$$

It is however worth noting that the exact physiological mechanism through which odorant clearance occurs in the respiratory epithelium (which does not contain ORNs) that covers the rostral end of the dorsal meatus is unknown at the present time. Nevertheless, regardless of the odorant clearance mechanism, this boundary condition is still physiologically realistic under the present set of assumptions because even if the consumption rate is slow, the effective odorant concentration is zero at the epithelial surface in the presence of a very weak odor signal.

The nondimensional parameter θ describes how readily odorant molecules are transported from the airstream to the epithelial surface. Thus, along with the nasal airflow patterns, θ values determine odorant deposition patterns in the nasal cavity during steady inspiration. For $\theta \gg 1$, equation (5) approaches a zero-concentration boundary condition, representing a highly soluble odorant that is instantly transported through the mucus layer and consumed at the epithelial surface. Conversely, for $\theta \to 0$, equation (5) becomes a zero-odorant-flux boundary condition, representing an odorant that is not absorbed into the mucus layer at all.

The odorant diffusion coefficients, D_{om} and D_{oa}, are similar for most odorants (see Table 1), and the mucus layer thickness, $h_m = 10$ μm (Menco 1980), is not expected to vary by more than a single order of magnitude. Accordingly, the value of the θ parameter is influenced primarily by the air–mucus partition coefficient, K_p, which spans 6 orders of magnitude for the odorants considered. Thus, while variations in the mucus layer thickness will slightly affect odorant deposition patterns, the effect is presumably insignificant because variations in K_p dominant changes in θ values.

As previously mentioned, preliminary simulations were performed to verify our assumption that odorant deposition in the respiratory airways has a negligible influence on odorant transport patterns in the dorsal meatus and the olfactory region. First, we simulated odorant transport in the nose and only modeled deposition along the dorsal meatus and in the olfactory region, as described above. We then simulated odorant transport in the nose and modeled deposition across all the nasal airways (using the boundary condition of eq. 5) with the exceptions of the frontal sinus and the nasal vestibule. The flow in the frontal sinus is nearly stagnant on inspiration and expiration (Craven et al. 2009, 2010), whereas the nasal vestibule is covered with squamous epithelium that has a low permeability in comparison to the olfactory and respiratory epithelium (Kimbell et al. 1997). Consequently, little odorant deposition should occur in the sinus and the nasal vestibule, and the little that does should have a negligible effect on deposition patterns in the other nasal airways.

The results from the 2 sets of simulation were quantitatively compared by calculating the total odorant uptake (i.e., absorption) by the dorsal meatus and the olfactory airways. The calculations showed that the differences in the total amount of odorant uptake between the 2 sets of simulations were less than 3% for amyl acetate, less than 6% for DNT, and less than 0.1% for limonene for all the flow rates considered, as Table 2 indicates. Although the results show that deposition in the respiratory airways has a small influence on the total amount of odorant uptake in the dorsal meatus and the olfactory region, it is possible that the deposition patterns are affected. To investigate this possibility, we visualized the air-phase odorant concentration through a representative transverse section of the olfactory region. Figure 5 presents this visualization for the airflow rate of 220 mL/s. There are no qualitative differences in the odorant transport patterns in the olfactory scroll work, where ORNs are located. The only noticeable differences between the 2 solutions are in the maxillary recess, which is anatomically separate from the olfactory region and has no olfactory function. Note that other transverse sections through the olfactory region show similar qualitative agreement, as do transverse sections from simulations of the other airflow rates that were considered (50 and 460 mL/s).

The results from the preliminary simulations show that deposition in the respiratory airways has very small qualitative and quantitative effects on odorant transport patterns in the olfactory region. Accordingly, the results presented in the remainder of this paper will be from simulations in which deposition in the respiratory airways was not modeled, as described above. Moreover, the preliminary results corroborate the findings from previous studies of canine nasal airflow that indicate respiratory and olfactory flow paths do not mix (Craven et al. 2009, 2010).

Table 2 The percent difference in odorant uptake by the dorsal meatus and the olfactory region between simulations where odorant deposition was modeled in the respiratory airways and simulations where a zero-odorant-flux boundary condition (eq. 4) was applied across the respiratory airways.

Airflow rate (mL/s)	% Difference in amyl acetate uptake	% Difference in DNT uptake	% Difference in limonene uptake
50	2.8	3.9	0.08
220	1.3	5.4	0.01
460	1.0	5.9	0.01

Results

Nasal airflow patterns

The canine nose is responsible for both respiratory and olfactory functions. As these 2 functions have unrelated objectives, it is not surprising that the nose has evolved separate flow paths for each (Craven et al. 2010). Figure 6 shows several inspiratory streamlines that reveal the existence of separate olfactory and respiratory airflow paths through the nasal cavity. Respiratory airflow exits the nasal vestibule and flows ventrally through the maxilloturbinate airway toward the nasopharynx, where it enters the lower respiratory tract, completely bypassing the olfactory recess.

The olfactory flow path is significantly more complex: a single airway (the dorsal meatus) transports odorant-laden airflow around the maxilloturbinate airway directly to the rear of the olfactory recess (see Figure 6). From there, the flow turns 180° and filters slowly forward through the more peripheral olfactory "scroll-work" toward the nasopharynx. The most significant distinction between the various olfactory streamlines is their residence time in the olfactory recess. In general, olfactory airflow that passes through the dorsal ethmoturbinates resides in the nasal cavity significantly longer than olfactory flow that passes through the ventral or lateral ethmoturbinate regions. Across all flow rates, olfactory airflow comprises approximately 15% of the total airflow inspired by the dog, the remainder going toward respiration. The flow patterns described above and shown in Figure 6 do not vary significantly as a function of the inspired airflow rate.

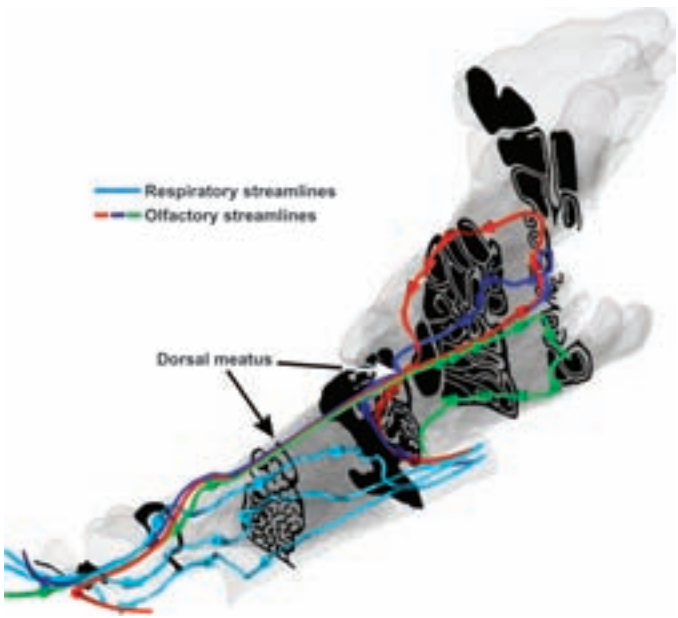

Figure 6 Inspiratory airflow patterns in the canine nasal cavity at peak inspiration (460 mL/s). Airflow enters the nose at the left through the nasal vestibule. The red, dark blue, and green streamlines illustrate the dorsal, lateral, and ventral olfactory flow paths, respectively. The arrowheads on the olfactory streamlines represent the direction of the airflow. The orientation of the nasal cavity is similar to that shown in Figure 1.

Present simulations show that nasal airflow patterns in the dog are similar to those previously reported for the rat (Morgan et al. 1991; Kimbell et al. 1997; Zhao et al. 2006; Yang, Scherer, and Mozell 2007). Specifically, the dog's nasal flow field has an s-shaped olfactory flow path similar to the flow path in the rat (the green streamline in Figure 6). In addition, the dog has a set of dorsal ethmoidal scroll work that is not present in the rat. This additional set of olfactory scroll work provides a dorsal olfactory flow path (the red streamline in Figure 6) that has not been observed in the rat.

Odorant deposition patterns in the canine olfactory recess

During steady inspiration, odorant flux to the olfactory epithelium determines the strength of an odor signal delivered to the ORNs. Figure 7 shows surface contours of odorant flux across the external surfaces of the nasal cavity on which mucus layer odorant transport was simulated. To give the odorant flux a physical significance, it is presented in units of molecules/ORN-s. The odorant flux was calculated using an ORN area density of 6.1×10^{10} ORNs/m^2 (Menco 1980), assuming an odorant inlet concentration of 1 nM/m^3, which is in the range of the detection threshold reported for the dog (Moulton and Marshall 1976; Walker et al. 2006). Note that the contour legends in Figure 7 vary over 4 orders of magnitude for the different odorants.

While the surface contours of Figure 7 illustrate the deposition patterns on external surfaces of the olfactory recess, the internal scroll-like surfaces remain obscured. Transverse sections of airstream concentration, presented in Figure 8, are the most effective method of visualizing odorant transport and deposition patterns in these internal airways. Figure 8 shows the nondimensional odorant concentration profiles for the 3 odorants considered at each flow rate simulated. Note that the surface concentration shown in Figure 8 is directly related to surface flux as described by equation (5).

At all flowrates and for all odorants, the largest odorant fluxes are observed along the dorsal meatus where the odorant concentration is highest. Odorant flux and air-phase concentration then decrease along the olfactory flow path as clearly shown in Figures 7 and 8. The rate at which the odorant flux and concentration decrease are directly related to the solubility of the odorant.

DNT, which is highly soluble, is quickly absorbed along the dorsal meatus near the entrance to the olfactory region (see Figures 7a and 8a–c). The olfactory airstream is therefore nearly depleted of DNT before the airflow reaches the rear of the olfactory recess and begins filtering forward.

Amyl acetate is moderately soluble in the mucus layer, so its deposition patterns are found to be highly dependent upon the olfactory flow path (see Figures 7b and 8d–f). Airflow that takes the short ventral path through the olfactory recess is not significantly depleted of amyl acetate. In contrast,

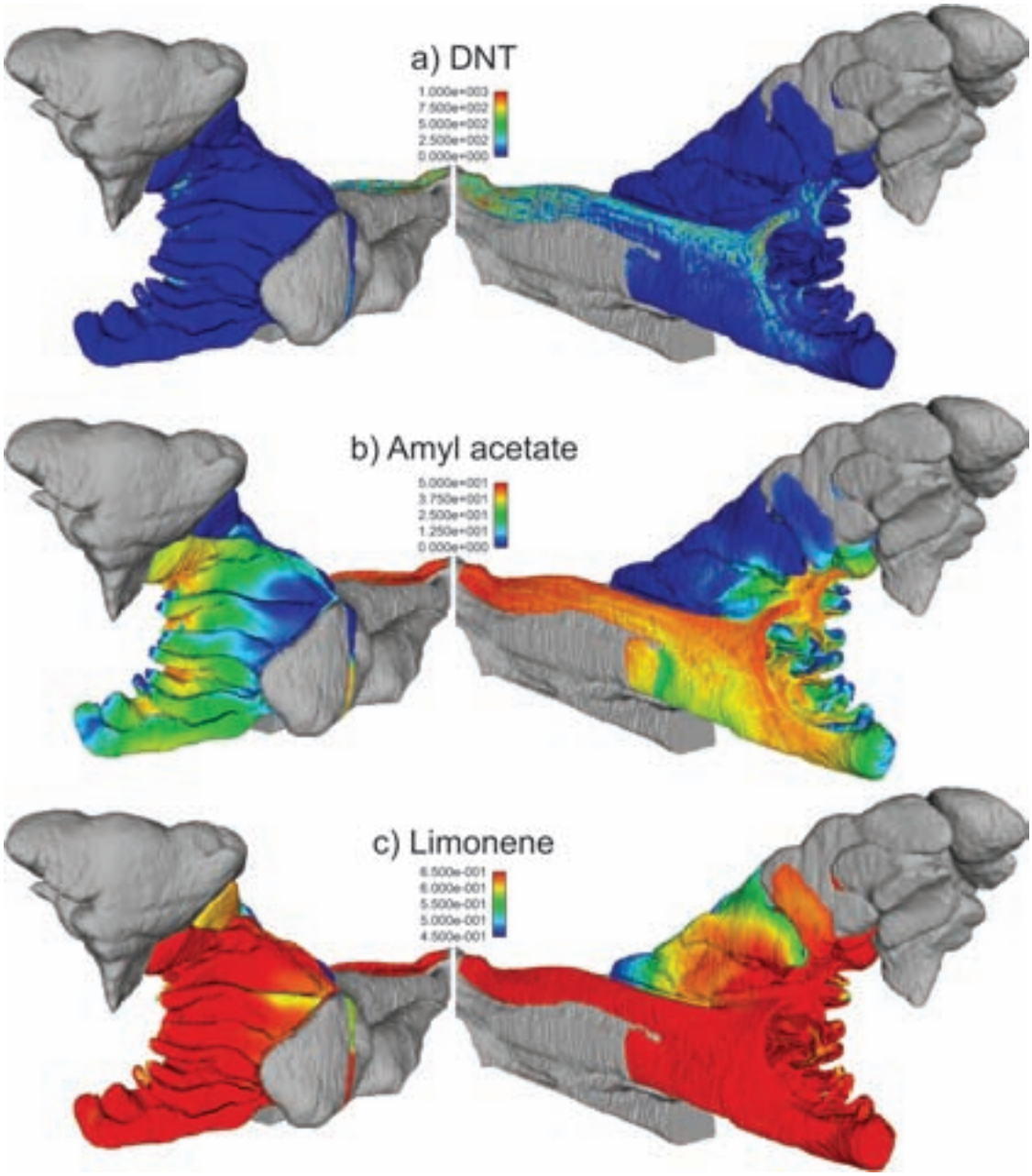

Figure 7 Surface contours of molecular flux to ORNs in the olfactory recess in units of molecules/ORN-s for (**a**) DNT, (**b**) amyl acetate, and (**c**) limonene at peak inspiration (460 mL/s). The left and right views in each panel show the olfactory recess viewed from lateral and medial perspectives, respectively. Nonolfactory surfaces are colored gray. As shown, the molecular flux to ORNs is nonuniform for (**a**) DNT and (**b**) amyl acetate, but it is roughly uniform for (**c**) limonene. Note that the contour legends vary over 4 orders of magnitude for the different odorants.

airflow taking the longer dorsal path is almost completely depleted of amyl acetate upon exiting the nasal cavity through the nasopharynx. The nonuniform absorption patterns for amyl acetate cause highly nonuniform odorant flux across the olfactory epithelium at all airflow rates.

Last, limonene is weakly absorbed by the mucus layer and the entire olfactory recess is exposed to nearly uniform limonene concentration, except at the lowest flowrate, at which there is significant limonene absorption along the dorsal meatus and nasal septum (see Figures 7c and 8g–i). Furthermore, as shown in Figure 7, limonene surface fluxes are low in relation to the other odorants considered due to limonene's large partition coefficient.

The effect of airflow rate on odorant deposition patterns

Nasal airflow rate also affects the deposition patterns as illustrated in Figure 8. This observation is quantified in Figure 9,

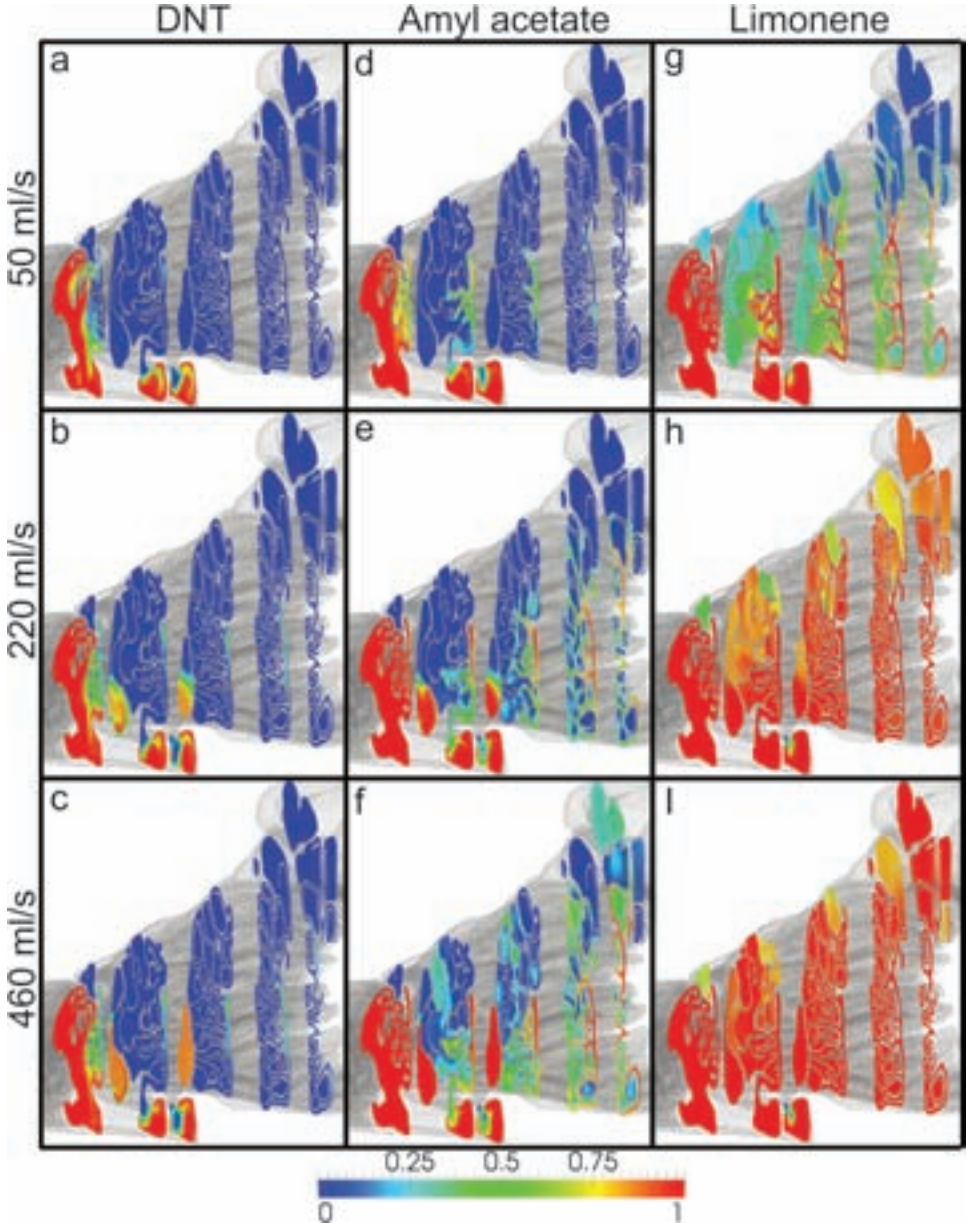

Figure 8 Transverse contours of nondimensional odorant concentration in the olfactory recess for: (**a**–**c**) DNT, (**d**–**f**) amyl acetate, and (**g**–**i**) limonene. Airflow rates of (**a**, **d**, **g**) 50 mL/s, (**b**, **e**, **h**) 220 mL/s, and (**c**, **f**, **i**) 460 mL/s are shown for each odorant. Note that the left-most transverse slice in each panel contains some nonolfactory airways (see Figure 1). Although the concentration in these nonolfactory airways is 1, odorant fluxes in nonolfactory airways were not simulated and therefore the odorant concentrations are meaningless outside the dorsal meatus and the olfactory recess.

which plots the total odorant uptake (the sum of the uptake of the dorsal meatus and the olfactory region) and the odorant uptake of only the dorsal meatus as a function of nasal airflow rate. Note that the odorant uptake of only the olfactory region is the difference between the total odorant uptake and the uptake along the dorsal meatus. At low flow rates, the dorsal meatus absorbs the majority of odorant before it reaches the more peripheral olfactory scroll work, epically for highly soluble odorants such as DNT. With increasing airflow rate, odorant-laden air is advected farther into the olfactory scroll work before the odorant becomes depleted from the airstream. In effect, increasing the nasal flow rate causes odorant molecules to be deposited across a larger percentage of the dog's olfactory surface area, while simultaneously increasing odorant surface flux. As shown in Figures 7 and 8, nasal flow rate has a large effect on deposition patterns of amyl acetate (moderately soluble) and limonene (insoluble), but has limited effect on the deposition patterns of DNT (highly soluble). Physically, this is because DNT is almost completely absorbed before it reaches peripheral olfactory scroll work, where variations in deposition patterns with changing flow rate are most apparent.

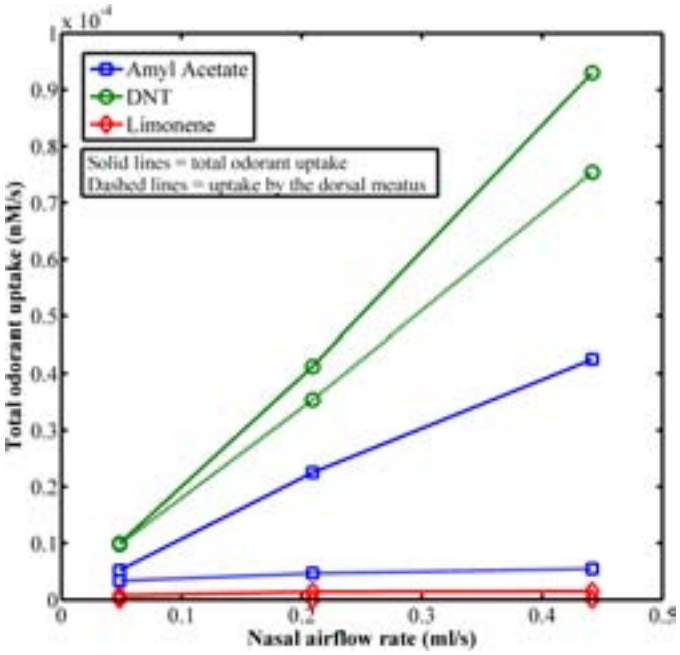

Figure 9 Total odorant uptake (i.e., uptake by the olfactory region and the dorsal meatus) and odorant uptake along the dorsal meatus as a function of nasal airflow rate. The amount of odorant uptake by the olfactory region is the difference between the total uptake and the dorsal meatus uptake. The odorant uptake values were calculated assuming the odorant concentration entering the nasal cavity was 1 nM/m^3, although, the y axis units are arbitrary due to the linear nature of equation (1).

To quantify the effect of partition coefficient and flow rate on deposition in the nasal cavity, we define a normalized odorant removal efficiency of the olfactory recess as:

$$\eta = 1 - \frac{J_{out}}{J_{in}}. \tag{7}$$

J_{in} and J_{out} are the airborne odorant fluxes into and out of the olfactory region, respectively. J_{in} was determined by calculating the total amount of odorant flux that entered the dorsal meatus. J_{out} was determined by integrating the odorant flux across the olfactory region and the dorsal meatus and subtracting the value from J_{in}.

A removal efficiency of 1 indicates that the odorant was completely absorbed in the olfactory recess. Figure 10 presents a plot of the removal efficiency for each odorant considered here as a function of the nasal airflow rate. The odorant removal efficiency is observed to increase rapidly with decreasing odorant partition coefficient. For example, at peak inspiration, the removal efficiency is 0.03 for limonene and 0.71 for DNT. Increasing the airflow rate has the effect of decreasing the removal efficiency for all odorants.

This trend is somewhat misleading, however, since the total odorant uptake increases significantly with airflow rate as illustrated by Figure 9. Thus, ''sniffing harder'' to increase nasal airflow rate decreases the removal efficiency of the olfactory recess but nonetheless provides a larger odorant flux to the ORNs. Behavioral evidence suggests that macrosmatic

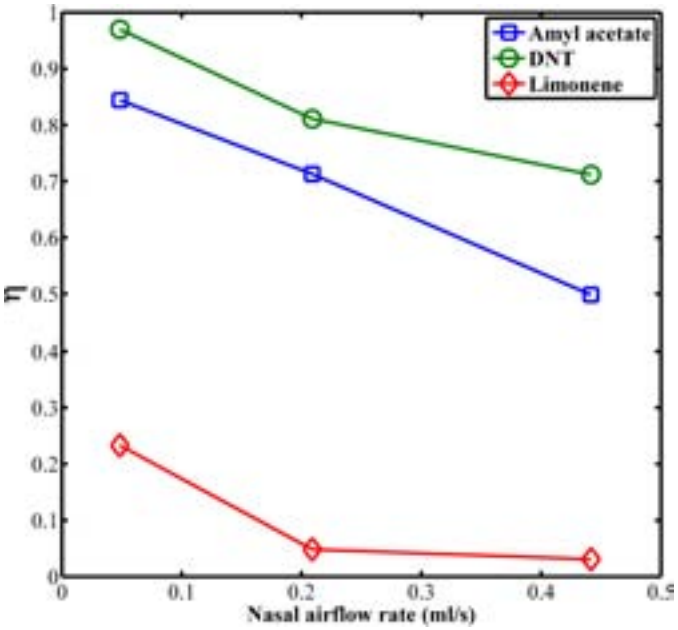

Figure 10 Normalized odorant removal efficiency (eq. 7) of the olfactory recess as a function of nasal airflow rate.

mammals may take advantage of this phenomenon by increasing their inspiratory flow rate to maximize odorant uptake when trying to detect low-concentration odors (Youngentob et al. 1987). This principle is also important to

bio-inspired "mechanical sniffer" designs for use in chemical trace detection applications (Settles 2005).

Comparison of the present results with odorant deposition patterns in the nasal cavity of the rat

For insoluble odorants, the present simulations predict significantly different deposition patterns than similar computational studies in the rat have reported (Zhao et al. 2006; Yang, Scherer, Zhao, et al. 2007). Yang, Scherer, Zhao, et al. (2007) found that insoluble odorants are deposited primarily on peripheral scroll-like olfactory surfaces. Whereas, as previously discussed, our results show that insoluble odorants are absorbed almost uniformly over all olfactory surfaces for airflow rates between 25% and 100% of the maximum inspiratory airflow rate. At very low nasal airflow rates (5% of the maximum value, see Figure 8g), we observe patterns opposite those reported by Yang, Scherer, Zhao, et al. (2007). Specifically, at low flow rates all of the odorants, including insoluble limonene, are absorbed appreciably in the dorsal meatus before the olfactory airflow turns 180° and filters back through the olfactory scroll work. Hence, at low nasal flow rates, we observed odorant flux to be higher along medial olfactory surfaces around the dorsal meatus than in the more peripheral olfactory scroll work.

Discussion

Correlation between odorant deposition patterns and ORN expression topography in macrosmatic mammals

Our results indicate that soluble and insoluble odorants are transported to the ORNs by different mechanisms. Highly soluble odorants, such as DNT, are deposited mainly along the dorsal meatus and nasal septum near the entrance to the olfactory recess (see Figure 8) where class I ORNs that are sensitive to highly soluble odorants are expressed. Moreover, because odorant-laden air is delivered to the olfactory recess via a high-velocity airstream in the dorsal meatus, odorant absorption on nonolfactory surfaces is less than if olfactory airflow were delivered via the maxilloturbinate airway, which serves the physiological purpose of exchanging heat and mass (i.e., particles and chemical compounds) between the inspired airflow and the surface of the nose for cooling and particle filtration reasons. Since the canine olfactory recess is located at the rear of the nasal cavity, this rapid transport mechanism appears to permit the detection of highly soluble odorants that would otherwise be absorbed prior to reaching the olfactory recess.

The mechanism through which moderately soluble and insoluble odorants are transported to ORNs is significantly different. Amyl acetate and limonene fluxes to the olfactory epithelium are significantly lower than the DNT flux as shown in Figures 8 and 10. However, amyl acetate and limonene are deposited more uniformly across the olfactory epithelium where class II ORNs that are likely sensitive to insoluble odorants are predominantly expressed. In effect, the dog's nose appears to utilize odorant absorption over a large surface area to compensate for the lower absorption rate of insoluble odorants. ORN density is approximately constant throughout the olfactory epithelium, so there are significantly more class II ORNs than class I ORNs in the nose (3 times as many for the rat according to Schoenfeld and Cleland 2006). Despite this, class I and class II ORNs converge to the same number of targets (glomeruli) in the olfactory bulb (Schoenfeld and Knott 2004; Schoenfeld and Cleland 2006). Thus, the high convergence ratio for class II ORNs and the absorption of insoluble odorants over the large olfactory surface area may act in concert to improve odorant "stimulus sensitivity" for insoluble odorants.

Most notably, odorant deposition patterns shown here correlate with ORN expression topography. ORNs that are sensitive to a particular class of odorants (soluble or insoluble) are located in regions where that class of odorants is deposited. The previously mentioned computational study of odorant transport in the rat's nose by Yang, Scherer, Zhao, et al. (2007) showed a similar result. This suggests that odorant deposition patterns play an important role in odor recognition, especially for low-concentration odors where the efficient delivery of odorant molecules to ORNs is critical.

Relation to behavioral observations

Behavioral observations in rats and dogs suggest that sniffing is actively controlled during olfaction (Zuschneid 1973; Youngentob et al. 1987; Settles 2005; Kepecs et al. 2007; Wesson, Carey, et al. 2008; Wesson, Donahou, et al. 2008; Craven et al. 2010). Youngentob et al. (1987) found that rats sniffed more vigorously when presented with a weak (low-concentration) odor signal. Sniffing harder increases the airstream velocity in the nasal vestibule and dorsal meatus, thus decreasing the fraction of the inspired odorant that is absorbed on these surfaces prior to the olfactory recess and increasing the total odorant flux to the olfactory recess (see Figure 9). Thus, it appears that macrosmatic mammals have evolved a sniffing strategy that provides a higher odorant flux to the ORNs in the presence of a weak odor signal.

Significance of the results to the design of bio-inspired artificial noses

Lessons from nature on the efficient aerodynamic design of an artificial olfaction device were earlier summarized by Settles (2005), especially the need for large sensor surface area and frictional pressure loss in order to allow odorant molecules the best opportunity of contacting the sensory epithelium. Here, we see the additional importance of a spatial odorant deposition pattern over this large sensor surface, with specialized ORNs presumably distributed across it for maximum advantage. This provides the dog an opportunity to separate the components of a complex scent, as in

chromatography, to improve neurological olfactory pattern recognition.

However, the compromise of olfaction and respiration in the limited volume of the dog's nose requires airborne conveyance of scents to the olfactory recess at the rear of the nasal cavity before olfaction can occur. The potential loss of trace chemicals to the walls of conveyance tubes is well known. Volatile odorants with small partition coefficients are the first to be absorbed by the mucosa, and some may not even reach the dog's olfactory epithelium. Dogs evolved to detect food and reproductive scents for survival and their olfactory region is relegated to the rear of the nasal cavity. Thus, it appears that the dog's nose is not optimized to detect highly soluble odorants (including some explosives), which are quickly absorbed upon entering the nasal cavity. Nonetheless, the lessons learned here can be applied to bio-inspired artificial noses, where a compromise with respiration is no longer required, and where the nose design can target the chemical properties of specific odorants of interest.

Conclusions

Large-scale CFD simulations were performed to study the effect of odorant solubility, nasal airflow patterns, and nasal airflow rate on odorant deposition patterns in the canine olfactory recess. Our simulations show that odorant-laden air is transported directly to the olfactory recess via a high-velocity airstream through the dorsal meatus, bypassing the more absorptive maxilloturbinate airway, thus decreasing odorant loss through absorption on nonolfactory surfaces. The highly soluble odorant DNT was observed to deposit primarily along the dorsal meatus and along the nasal septum near the entrance to the olfactory region. Moderately soluble amyl acetate and insoluble limonene were more evenly deposited across the olfactory epithelium and their deposition patterns were influenced by both the olfactory airflow pattern and the nasal airflow rate.

Odorant deposition patterns were found to correspond with ORN expression topography. Specifically, highly soluble odorants are deposited in the olfactory region along the dorsal meatus where class I ORNs (sensitive to highly soluble odorants) are expressed, whereas insoluble odorants are deposited across the entire olfactory recess where class II ORNs (sensitive to insoluble odorants) are predominately expressed. These results suggest that the nasal anatomy of the dog (and likely other macrosmatic animals) has evolved to provide odorant deposition patterns that complement the anatomical organization of ORNs in such a way as to enhance olfactory sensitivity and odor recognition abilities.

Funding

This work was supported by the United States National Defence Science and Engineering Graduate (NDSEG) Fellowship Program.

References

Bhandawat V, Reisert J, Yau KW. 2005. Elementary response of olfactory receptor neurons to odorants. Science. 308:1931–1934.

Briand L, Eloit C, Nespoulous C, Bézirard V, Huet JC, Henry C, Blon F, Trotier D, Pernollet JC. 2002. Evidence of an odorant-binding protein in the human olfactory mucus: location, structural characterization, and odorant-binding properties. Biochemistry. 41:7241–7252.

Buck L, Axel R. 1991. A novel multigene family may encode odorant receptors: a molecular basis for odor recognition. Cell. 65:175–187.

Craven BA. 2008. A fundamental study of the anatomy, aerodynamics, and transport phenomena of canine olfaction [PhD thesis]. University Park (PA): The Pennsylvania State University.

Craven BA, Neuberger T, Paterson EG, Webb AG, Josephson EM, Morrison EE, Settles GS. 2007. Reconstruction and morphometric analysis of the nasal airway of the dog (Canis familiaris) and implications regarding olfactory airflow. Anat Rec. 290:1325–1340.

Craven BA, Paterson EG, Settles GS. 2010. The fluid dynamics of canine olfaction: a new explanation for macrosmia. J R Soc Interface. 1:1–11.

Craven BA, Paterson EG, Settles GS, Lawson MJ. 2009. Development and verification of a high-fidelity computational fluid dynamics model of canine nasal airflow. J Biomech Eng. 131:091002.

Evans HE, Miller ME. 1993. Miller's anatomy of the dog. Philadelphia (PA): W.B. Saunders.

Hahn I, Scherer PW, Mozell MM. 1994. A mass transport model of olfaction. J Theor Biol. 167:115–128.

Hughes T, Franca L, Balestra M. 1986. A new finite element formulation for computational fluid dynamics. V: circumventing the Babuska-Brezzi condition: a stable Petrov-Galerkin formulation of the Stokes problem accommodating equal-order interpolations. Comput Methods Appl Mech Eng. 59:85–99.

Kauer JS, White J. 2001. Imaging and coding in the olfactory system. Annu Rev Neurosci. 24:963–979.

Kent PF, Mozell MM. 1992. The recording of odorant-induced mucosal activity patterns with a voltage-sensitive dye. J Neurophysiol. 68:1804–1819.

Kent PF, Mozell MM, Murphy SJ, Hornung DE. 1996. The interaction of imposed and inherent olfactory mucosal activity patterns and their composite representation in a mammalian species using voltage-sensitive dyes. J Neurosci. 16:345–353.

Kent PF, Mozell MM, Youngentob SL, Yurco P. 2003. Mucosal activity patterns as a basis for olfactory discrimination: comparing behavior and optical recordings. Brain Res. 981:1–11.

Kepecs A, Uchida N, Mainen ZF. 2007. Rapid and precise control of sniffing during olfactory discrimination in rats. J Neurophysiol. 98:205–213.

Keyhani K, Scherer PW, Mozell MM. 1995. Numerical simulation of airflow in the human nasal cavity. J Biomech Eng. 117:429–441.

Keyhani K, Scherer PW, Mozell MM. 1997. A numerical model of nasal odorant transport for the analysis of human olfaction. J Theor Biol. 186:279–301.

Kimbell JS, Godo MN, Gross EA, Joyner DR, Richardson RB, Morgan KT. 1997. Computer simulation of inspiratory airflow in all regions of the F344 rat nasal passages. Toxicol Appl Pharmacol. 145:388–398.

Kimbell JS, Gross EA, Joyner DR, Godo MN, Morgan KT. 1993. Application of computational fluid dynamics to regional dosimetry of inhaled chemicals in the upper respiratory tract of the rat. Toxicol Appl Pharmacol. 121:253–263.

Kimbell JS, Subramaniam RP, Gross EA, Schlosser PM, Morgan KT. 2001. Dosimetry modeling of inhaled formaldehyde: comparisons of local flux predictions in the rat, monkey, and human nasal passages. Toxicol Sci. 64:100–110.

Kurtz DB, Zhao K, Hornung DE, Scherer P. 2004. Experimental and numerical determination of odorant solubility in nasal and olfactory mucosa. Chem Senses. 29:763–773.

Menco BP. 1980. Qualitative and quantitative freeze-fracture studies on olfactory and nasal respiratory structures of frog, ox, rat, and dog. I. A general survey. Cell Tissue Res. 207:183–209.

Mezler M, Fleischer J, Breer H. 2001. Characteristic features and ligand specificity of the two olfactory receptor classes from Xenopus laevis. J Exp Biol. 204:2987–2997.

Miyamichi K, Serizawa S, Kimura H, Sakano H. 2005. Continuous and overlapping expression domains of odorant receptor genes in the olfactory epithelium determine the dorsal/ventral positioning of glomeruli in the olfactory bulb. J Neurosci. 25:3586–3592.

Mombaerts P, Wang F, Dulac C, Chao SK, Nemes A, Mendelsohn M, Edmondson J, Axel R. 1996. Visualizing an olfactory sensory map. Cell. 87:675–686.

Morgan KT, Kimbell JS, Monticello TM, Patra AL, Fleishman A. 1991. Studies of inspiratory airflow patterns in the nasal passages of the F344 rat and rhesus monkey using nasal molds: relevance to formaldehyde toxicity. Toxicol Appl Pharmacol. 110:223–240.

Moulton D. 1976. Spatial patterning of response to odors in the peripheral olfactory system. Physiol Rev. 56:578–593.

Moulton D, Marshall D. 1976. The performance of dogs in detecting alpha-ionone in the vapor phase. J Comp Physiol A. 110:287–306.

Mozell M, Kent P, Murphy S. 1991. The effect of flow rate upon the magnitude of the olfactory response differs for different odorants. Chem Senses. 16:631–649.

Mozell MM. 1964. Evidence for sorption as a mechanism of the olfactory analysis of vapours. Nature. 203:1181–1182.

Mozell MM. 1966. The spatiotemporal analysis of odorants at the level of the olfactory receptor sheet. J Gen Physiol. 50:25–41.

Mozell MM. 1970. Evidence for a chromatographic model of olfaction. J Gen Physiol. 56:46–63.

Mozell MM, Sheehe PR, Hornung DE, Kent PF, Youngentob SL, Murphy SJ. 1987. "Imposed" and "inherent" mucosal activity patterns. Their composite representation of olfactory stimuli. J Gen Physiol. 90: 625–650.

Nef P, Hermans-Borgmeyer I, Artières-Pin H, Beasley L, Dionne VE, Heinemann SF. 1992. Spatial pattern of receptor expression in the olfactory epithelium. Proc Natl Acad Sci U S A. 89:8948–8952.

Negus V. 1958. The comparative anatomy and physiology of the nose and paranasal sinuses. London: Livingstone.

Pelosi P. 1996. Perireceptor events in olfaction. J Neurobiol. 30:3–19.

Quignon P, Giraud M, Rimbault M, Lavigne P, Tacher S, Morin E, Retout E, Valin AS, Lindblad-Toh K, Nicolas J, et al. 2005. The dog and rat olfactory receptor repertoires. Genome Biol. 6:R83.

Ressler KJ, Sullivan SL, Buck LB. 1993. A zonal organization of odorant receptor gene expression in the olfactory epithelium. Cell. 73:597–609.

Schoenfeld TA, Cleland TA. 2005. The anatomical logic of smell. Trends Neurosci. 28:620–627.

Schoenfeld TA, Cleland TA. 2006. Anatomical contributions to odorant sampling and representation in rodents: zoning in on sniffing behavior. Chem Senses. 31:131–144.

Schoenfeld TA, Knott TK. 2004. Evidence for the disproportionate mapping of olfactory airspace onto the main olfactory bulb of the hamster. J Comp Neurol. 476:186–201.

Scott JW, Acevedo HP, Sherrill L. 2006. Effects of concentration and sniff flow rate on the rat electroolfactogram. Chem Senses. 31:581–593.

Settles G. 2005. Sniffers: fluid-dynamic sampling for olfactory trace detection in nature and homeland security—the 2004 freeman scholar lecture. J Fluids Eng. 127:189–218.

Shakib F. 1989. Finite element analysis of the compressible Euler and Navier-Stokes equations [PhD thesis]. [Stanford (CA)]: Stanford University Stanford.

Steinbrecht RA. 1998. Odorant-binding proteins: expression and function. Ann N Y Acad Sci. 855:323–332.

Strotmann J, Wanner I, Helfrich T, Beck A, Breer H. 1994. Rostro-caudal patterning of receptor-expressing olfactory neurones in the rat nasal cavity. Cell Tissue Res. 278:11–20.

Truskey G, Yuan F, Katz D. 2008. Transport phenomena in biological systems. Upper Saddle River (NJ): Prentice Hall.

Vassar R, Ngai J, Axel R. 1993. Spatial segregation of odorant receptor expression in the mammalian olfactory epithelium. Cell. 74:309–318.

Walker D, Walker J, Cavnar P, Taylor J, Pickel D, Hall S, Suarez J. 2006. Naturalistic quantification of canine olfactory sensitivity. Appl Anim Behav Sci. 97:241–254.

Wesson DW, Carey RM, Verhagen JV, Wachowiak M. 2008. Rapid encoding and perception of novel odors in the rat. PLoS Biol. 6:717–729.

Wesson DW, Donahou TN, Johnson MO, Wachowiak M. 2008. Sniffing behavior of mice during performance in odor-guided tasks. Chem Senses. 33:581–596.

Yang GC, Scherer PW, Mozell MM. 2007. Modeling inspiratory and expiratory steady-state velocity fields in the Sprague-Dawley rat nasal cavity. Chem Senses. 32:215–223.

Yang GC, Scherer PW, Zhao K, Mozell MM. 2007. Numerical modeling of odorant uptake in the rat nasal cavity. Chem Senses. 32:273–284.

Youngentob S, Mozell M, Sheehe P, Hornung D. 1987. A quantitative analysis of sniffing strategies in rats performing odor detection tasks. Physiol Behav. 41:59–69.

Zhang X, Firestein S. 2002. The olfactory receptor gene superfamily of the mouse. Nat Neurosci. 5:124–133.

Zhang X, Rogers M, Tian H, Zhang X, Zou DJ, Liu J, Ma M, Shepherd GM, Firestein SJ. 2004. High-throughput microarray detection of olfactory receptor gene expression in the mouse. Proc Natl Acad Sci U S A. 101:14168–14173.

Zhao K, Dalton P, Yang GC, Scherer PW. 2006. Numerical modeling of turbulent and laminar airflow and odorant transport during sniffing in the human and rat nose. Chem Senses. 31:107–118.

Zhao K, Scherer PW, Hajiloo SA, Dalton P. 2004. Effect of anatomy on human nasal air flow and odorant transport patterns: implications for olfaction. Chem Senses. 29:365–379.

Zuschneid K. 1973. The olfactory acuity of the dog (Die Riechleistung Des Hundes) [PhD thesis]. [Berlin (Germany)]: Free University of Berlin.